Monthly Notices of the ROYAL ASTRONOMICAL SOCIETY

MNRAS **520,** 2747–2756 (2023) https://doi.org/10.1093/mnras/stad194
Advance Access publication 2023 January 20

Single-pulse studies of three millisecond pulsars

N. T. Palliyaguru [1]★ B. B. P. Perera [2]★ M. A. McLaughlin [3,4] S. Osłowski [5] and G. L. Siebert[6]

[1]*Department of Physics and Astronomy, Texas Tech University, Lubbock, TX 79409, USA*
[2]*Arecibo Observatory, University of Central Florida, HC3 Box 53995, Arecibo, PR 00612, USA*
[3]*Department of Physics and Astronomy, West Virginia University, Morgantown, WV 26501, USA*
[4]*Center for Gravitational Waves and Cosmology, West Virginia University, Chestnut Ridge Research Building, Morgantown, WV 26505, USA*
[5]*Manly Astrophysics, 15/41-42 East Esplanade, Manly, NSW 2095, Australia*
[6]*Department of Physics, University of Wisconsin Madison, Madison, WI 53703, USA*

Accepted 2023 January 13. Received 2022 December 28; in original form 2021 December 24

ABSTRACT

Single-pulse studies are important to understand the pulsar emission mechanism and the noise floor in precision timing. We study total intensity and polarimetry properties of three bright millisecond pulsars – PSRs J1022+1001, J1713+0747, and B1855+09 – that have detectable single pulses at multiple frequencies. We report for the first time the detection of single pulses from PSRs J1022+1001 and J1713+0747 at 4.5 GHz. In addition, for those two pulsars, the fraction of linear polarization in the average profile is significantly reduced at 4.5 GHz, compared to 1.38 GHz, which could support the expected deviation from a dipolar field closer to the pulsar surface. There is a hint of orthogonal modes in the single pulses of PSR J1713+0747. More sensitive multifrequency observations may be useful to confirm these findings. The jitter noise contributions at 1.38 GHz, scaled to one hour, for PSRs J1022+1001, J1713+0747, and B1855+09 are ≈135, ≈45, and ≈60 ns, respectively and are consistent with previous studies. We also show that selective bright-pulse timing of PSR J1022+1001 yields improved root-mean-square residuals of ≈22 μs, which is a factor of ≈3 better than timing using single pulses alone.

Key words: stars: neutron – pulsars: general – pulsars: individual: PSR J1022+1001, J1713+0747, B1855+09.

1 INTRODUCTION

In general, pulsar emission remains poorly understood. The commonly accepted model suggests that emission is produced by curvature radiation from bunches of charged particles moving along magnetic field lines at relativistic speeds. The emitted photons split into electron–positron pairs, producing a cascade of secondary pair plasma (Goldreich & Julian 1969; Ruderman & Sutherland 1975). Components of the electric field that are parallel ($E_{\parallel}$) and perpendicular ($E_{\perp}$) to the magnetic field lines produce highly linearly polarized emission. Circular polarization is thought to be generated both by intrinsic mechanisms and/or by propagation effects within the magnetosphere (Melrose 1995), where a time delay is introduced between $E_{\parallel}$ and $E_{\perp}$ due to different refractive indices of the two orthogonal components in the magnetosphere (Gil & Snakowski 1990). As the pulsar beam crosses our line of sight, sweeping through different magnetic field lines, the polarization position angle (PPA), which is the angle between the magnetic field line and the fiducial plane (i.e. the plane passing through the rotation and magnetic axes) makes an S-shaped curve (Radhakrishnan & Cooke 1969). The PPA information is utilized in constraining the geometry of pulsars using the rotating vector model (e.g. Rankin 1983a,b; Mitra & Rankin 2011).

Millisecond pulsars (MSPs) are old neutron stars that are spun up to millisecond periods. They have smaller magnetospheres and relatively smaller (∼four orders of magnitude) magnetic field strengths than canonical pulsars, which have not been through the recycling process (Lorimer & Kramer 2012). This poses the question of whether emission of MSPs is different from canonical pulsars. For example, the emission beam size of a canonical pulsar is correlated with its period but such a correlation cannot be clearly seen for MSPs (Kramer et al. 1998). In addition, MSP profiles appear to show less evolution with frequency than those of canonical pulsars (Kramer et al. 1998). Some properties of canonical and millisecond pulsars are similar, however. For instance, MSPs can emit giant pulses (Heiles & Campbell 1970), like normal pulsars; there is evidence that giant pulses are linked to high magnetic field strengths at the pulsar light cylinder and to high-energy emission (Romani & Johnston 2001; Enoto et al. 2021). MSPs too may show a deviation from the dipolar field line structure close to the NS surface (e.g. Kramer et al. 1998; Gil, Melikidze & Mitra 2002; Kalapotharakos et al. 2021).

Pulsar emission is extremely complex, requiring sophisticated models to explain observations that do not fit into the general picture. Average pulse profiles are stable in general, with some notable exceptions, such as PSRs J1713+0747 (Brook et al. 2018; Xu et al. 2021), B1937+21 (Brook et al. 2018), and PSR B1828−11 (Lyne et al. 2010). However, emission is highly variable at a single-pulse level. Phenomena such as giant pulses (Heiles & Campbell 1970), mode changing (Backer 1970), drifting sub-pulses (Frake F. & Craft 1968; Backer 1973), nulling (Rankin 1986), and microstructure within single pulses (Cordes, Weisberg & Hankins 1990) are not

★ E-mail: nipunipalliyaguru9@gmail.com (NP); bhakthiperera@gmail.com (BP)

easily explained by a simple emission model. The PPAs of many pulsars, in particular MSPs, deviate from the S-shaped sweep and show discontinuities or unexpected jumps. These are sometimes separated by 90°, named orthogonal polarization modes (OPMs), and may result from either two highly polarized orthogonal modes of emission (e.g. Backer, Rankin & Campbell 1976; Cordes, Rankin & Backer 1978) or propagation effects (McKinnon & Stinebring 2000). Even though the curvature radiation with bunches explains the radio emission of pulsars to some extent, it has serious drawbacks, including the inability to explain the production of bunches and their existence over the characteristic time of emission (Melrose 1992). Furthermore, secondary pair plasma is insufficient to reach the charge density required by Maxwell's equations (e.g. Melrose 1995). As alternative mechanisms, relativistic plasma emission (Melrose & Gedalin 1999), anomalous Doppler emission (e.g. Machabeli & Usov 1979), linear acceleration emission (Cocke 1973), and maser emission (Zhelezniakov & Shaposhnikov 1979) have been proposed (see Melrose, Rafat M. & Mastrano 2021, for a review of these effects). However, none of these theoretical methods are capable of fully explaining the pulsar emission mechanism (Melrose 1995; Melrose et al. 2021). Single-pulse studies can provide valuable diagnostics of emission mechanisms. For example, Crab pulsar microstructures suggest coherent emission from strong plasma turbulence (Hankins & Eilek 2007). Also, highly polarized single pulses have been used to distinguish between coherent curvature radiation and maser emission in the past (Mitra, Gil & Melikidze 2009). Therefore, single-pulse studies, including single-pulse polarimetry, of pulsars with a variety of properties are crucial to fully understand pulsar emission physics (Rankin 1986).

MSPs are also important for low-frequency, from nHz to μHz, gravitational wave detection experiments through pulsar timing arrays (PTAs), which require precise measurements of pulse times of arrival (TOAs) and sub-microsecond timing accuracy (Desvignes et al. 2016; Perera et al. 2018, 2019; Kerr et al. 2020; Alam et al. 2021). Pulse-to-pulse jitter, profile variations, variation in polarization properties, and polarization calibration errors are among phenomena that could affect the precision of TOAs (Cordes & Shannon 2010; Liu et al. 2011; Osłowski et al. 2013). These can contribute to noise that can limit the timing precision of MSPs and therefore sensitivity of PTAs to gravitational waves. Therefore, studying MSPs at a single-pulse level to understand the contributions of these various phenomena can offer useful insights.

Single-pulse studies of MSPs have been sparse due to signal-to-noise ratio limitations due to their low fluxes (Kramer et al. 1998) and data acquisition requirements such as the need for high-time resolution sampling. The few previous studies have revealed highly linearly polarized single pulses and sub-pulse microstructure in J0437−4715 (Jenet et al. 1998; Osłowski et al. 2014; De, Gupta & Sharma 2016), giant pulses from B1937+21 (McKee et al. 2019), pulse jittering from PSR J1713+0747 (Shannon & Cordes 2012) and PSR J1022+1001 (Liu et al. 2015; Feng et al. 2020), and sub-pulse drifting from PSR J1713+0747 (Liu et al. 2015).

Polarization information in single pulses could get lost when averaging, causing depolarization in averaged pulse profiles (Backer & Rankin 1980). Therefore, studying single pulses may provide clues to the emission physics of pulsars. In addition to emission mechanisms, there are other advantages to performing polarimetry. Britton (2000) suggested the possibility of using invariant profiles to avoid errors due to calibration and van Straten (2006) suggested the use of polarimetric profiles to improve timing. Furthermore, Osłowski et al. (2013) used polarization information to correct for pulse-to-pulse variability in PSR J0437−4715, which resulted in a 40 per cent improvement in the timing precision of the pulsar. In light of these ideas, we investigate single-pulse emission properties in three stable millisecond pulsars – PSRs J1022+1001, J1713+0747, and B1855+09 – which are monitored regularly by PTAs (see Perera et al. 2019). PSR J1022+1001 is known to show long-term profile instabilities (e.g. Kramer et al. 1999; Liu et al. 2015; Padmanabh et al. 2021) and PSR J1713+0747 recently underwent a significant pulse shape change (e.g. Xu et al. 2021). While the origin of such changes is likely intrinsic, and not due to incorrect calibration, these events can introduce variations in timing residuals, degrading the PTA sensitivity to gravitational waves.

The paper is structured as follows. The details of observations and data processing are presented in Section 2. Data analysis techniques are presented in Section 3 and results are presented in Section 4. The conclusion and discussion of the study are presented in Section 5.

Table 1. Properties of the observed pulsars: The pulsar period, period derivative, the dispersion measure, and references.

Name	Period (ms)	$\dot{P}$ ($s\,s^{-1}$)	DM ($cm^{-3}\,pc$)	Reference
J1022+1001	16.453	4.334×10^{-20}	10.252	1,2
J1713+0747	4.570	8.530×10^{-21}	15.917	3,4
B1855+09	5.362	1.784×10^{-20}	13.314	4

Note. References: (1) Hotan, Bailes & Ord (2006), (2) Reardon et al. (2016), (3) Zhu et al. (2015), (4) Arzoumanian et al. (2018).

2 OBSERVATIONS AND DATA PROCESSING

PSRs J1022+1001, J1713+0747, and B1855+09 were observed with the 305-m William E. Gordon Telescope at the Arecibo observatory in Puerto Rico. The basic parameters of these three millisecond pulsars[1] are given in Table 1. Arecibo observations were carried out between 2018 August 5 and 2019 August 25. Data were recorded using the Puerto Rico Ultimate Pulsar Processing Instrument (PUPPI) at centre frequencies of 430, 1380, 2030, and 4500 MHz in full Stokes mode with 8bit sampling. Our multifrequency observation details, including the usable bandwidth, number of channels across the usable bandwidth, and the sampling time, for each pulsar, are listed in Table 2. The usable bandwidth at 1.38 and 2.3 GHz is less than the full receiver bandwidth due to radio frequency interference (RFI). While baseband recording mode allows higher time resolution, we accumulated data in search mode in order to maximize the available bandwidth and thereby to improve the S/N of the pulsar data. PSRs J1713+0747 and B1855+09 data were coherently dedispersed using DSPSR[2] (van Straten & Bailes 2011) at the dispersion measure listed in Table 2. PSR J1022+1001 was observed in the incoherent search mode. Each observation session started with a noise calibrator injection scan followed by the pulsar observation.

The recorded data were processed with DSPSR (van Straten & Bailes 2011) to obtain single pulses, which were further processed with PSRCHIVE[3] routines (Hotan, van Straten & Manchester 2004). The data from each pulsar were processed with 512 pulse phase bins given the time resolution used in the observation set-up. The automatic median zapping algorithms of PSRCHIVE were used

[1] https://www.atnf.csiro.au/research/pulsar/psrcat/
[2] http://dspsr.sourceforge.net
[3] http://psrchive.sourceforge.net

Table 2. Observation information, including MJD, frequency, observation length, bandwidth, number of channels across the bandwidth, sampling time, receiver temperature, sky temperature, measured rotation measures (published rotation measures are given in parentheses), equivalent width, measured mean flux density from the radiometer equation, and the number (and fraction) of pulses detected (S/N > 5).

Name	MJD	ν (MHz)	Length (s)	BW (MHz)	N_{chan}	G K/Jy	t_{samp} (μs)	T_{rec} (K)	T_{sky} (K)	RM (rad m^{-2})	W_{eq} (ms)	S_{mean} (mJy)	N
J1022+1001	58335	1380	300	600	384	8	20.48	30	0.62	5.31 ± 0.04 (–0.3, 2.18)	1.028 ± 0.002	4.89 ± 0.15	10755 (≈ 59%)
	58651	4500	1800	800	512	4	40.96	30	0.03	–	0.577 ± 0.003	0.90 ± 0.11	1175 (≈ 1%)
J1713+0747	58697	1380	300	600	384	8	10.24	30	2.92	10.69 ± 0.04 (13 ± 2)	0.1752 ± 0.0003	10.18 ± 0.17	64458 (≈ 98%)
	58697	4500	300	800	512	4	10.24	30	0.14	–	0.195 ± 0.002	1.37 ± 0.27	53 (≈ 0.08%)
B1855+09	58720	430	600	20	64	11	2.56	50	109.9	–	0.53 ± 0.01	10.61 ± 2.15	–
	58720	1380	1200	600	384	8	10.24	30	5.11	24.99 ± 0.18 (20 ± 4)	0.483 ± 0.001	5.21 ± 0.09	11480 (≈ 10%)
	58720	2030	600	460	384	8	10.24	40	1.94	–	0.43 ± 0.02	0.39 ± 0.17	–

Notes.
The published RM values are obtained from Yan et al. (2011), Noutsos et al. (2015), and Gentile et al. (2018).
The RM of PSR B1855+09 is not calculated at 430 MHz due to the small bandwidth.
T_{rec} and Gain values for AO are obtained from http://www.naic.edu/~astro/RXstatus/rcvrtabz.shtml.
T_{sky} in the direction of the pulsar is calculated according to Haslam et al. (1982).

to remove narrow-band and impulsive RFI. Remaining RFI was removed by visual inspection.

Polarization calibration was performed to correct for the differential gain and phase between the two polarization channels of the receiver due to imperfections in the amplifiers and mismatch between the cable chains along the two paths, assuming an ideal feed. For this, we used the calibrator scan which is a 25 Hz winking cal signal injecting a fully linearly polarized signal in between the two polarization probes at a 45° position angle. Next, the instrumental response was determined using polarization calibration modelling (pcm) as outlined in Britton (2000), assuming equal ellipticities of receptors. A flux calibrator was not observed during these observations. The polarization properties of the integrated profiles are shown in Fig. 1, which are consistent with previously published profiles (Dai et al. 2015).

Faraday rotation due to the magnetized ISM and the ionosphere causes a change in the PPA with frequency (e.g. Simard-Normandin & Kronberg 1980; Lyne & Smith 1989). The change in the PPA due to Faraday rotation is given by

$$\Delta\Psi = \lambda^2 \times \mathrm{RM}, \tag{1}$$

where λ is the observation wavelength. The rotation measure (RM), which depends on the average magnetic field and the electron density along the line of sight, was calculated using the RMFIT program in PSRCHIVE, which searches for a peak in the linear polarization for trial RMs. The best-fitting RM values (published values in parenthesis) are given in Table 2. Given the λ^2 dependence in equation (1), and the decrease in flux density with increasing frequency, the sensitivity to the change in the PPA decreases with increasing frequency. Therefore, the RM values derived from 1.38 GHz data were used to correct the data at higher frequencies.

Our RM values at 1.38 GHz are consistent within errors with published values for MSPs J1713+0747 and B1855+09 (see Table 2). However, significant trends in the measured RM have been observed for PSR J1713+0747 previously (Wahl et al. 2021). Our measured RM for PSR J1022+1001 differs significantly from its published value, however, PSR J1022+1001 is known to show changes in the RM when passing close to the sun i.e. when the angular separation between the pulsar and the sun is <3° (You et al. 2012) and also shows significant long-term RM variations (Yan et al. 2011). The angular separation between the sun and the pulsar was ≈15° during the 1.38 GHz observations. While it is not possible to pinpoint to the reason for the discrepancy between our measured and previously published RM values for PSR J1022+1001, we note that Noutsos et al. (2015), Feng et al. (2020), and Dai et al. (2015) also find higher RM values of 2.18(2), 2.9(2), and 4.68(6) rad m^{-2}, respectively.

For the pulse phase jitter analysis, average profiles of 50, 100, 200, 500, and 1000 pulses were created. A TOA for each profile was generated by cross-correlating it against a noise-free template profile. This template was obtained by fitting Gaussian components to a high S/N profile obtained by averaging over the full observation for a given frequency. Timing residuals were obtained using the TEMPO2 pulsar timing package (Edwards, Hobbs & Manchester 2006; Hobbs, Edwards & Manchester 2006). The timing ephemerides are obtained from data published in Perera et al. (2019).

3 DATA ANALYSIS

In this section, we discuss the data analysis tools used to measure total intensity properties, polarimetry of single pulses, and pulse phase jitter of PSRs J1022+1001, J1713+0747, and B1855+09.

Table 2 lists the measured equivalent pulse width W_{eq} and the measured flux density S_{mean} of the average profile over the full observation length from our multifrequency observations. W_{eq} is defined as the width of a top hat pulse with the peak amplitude I_{peak} and the same area as the on-pulse region and is calculated as

$$W_{eq} = \frac{\sum_{i=n_1}^{N} I_i}{I_{peak}}, \tag{2}$$

where I_i is the intensity of the ith bin of the on-pulse region ranging from bins n_1 to N in baseline-corrected data. The error of W_{eq} is calculated by applying error propagation on equation (2) and using the off and on-pulse rms as the errors of I_i and I_{peak}, respectively.

From the radiometer equation, the root mean square noise fluctuation is given by

$$\Delta S_{sys} = \frac{T_{sys}}{G\sqrt{N_p\, t_{obs}\, \Delta\nu}} = \mathrm{C}\,\sigma_p. \tag{3}$$

Here, C is the scaling factor, σ_p is the standard deviation of the off-pulse region, T_{sys} is the system temperature, which is the sum of the sky temperature (T_{sky}), the receiver temperature (T_{rec}), and the telescope spill over, G is the telescope gain, $\Delta\nu$ is the bandwidth, t_{obs} is the observation length, and $N_p = 2$ is the number of polarization channels (see Lorimer & Kramer 2012). The measured mean flux density S_{mean} is calculated by scaling the profile by C (i.e. $\Delta S_{sys}/\sigma_p$). The values for T_{rec}, T_{sky}, and G for different frequencies are listed in Table 2.

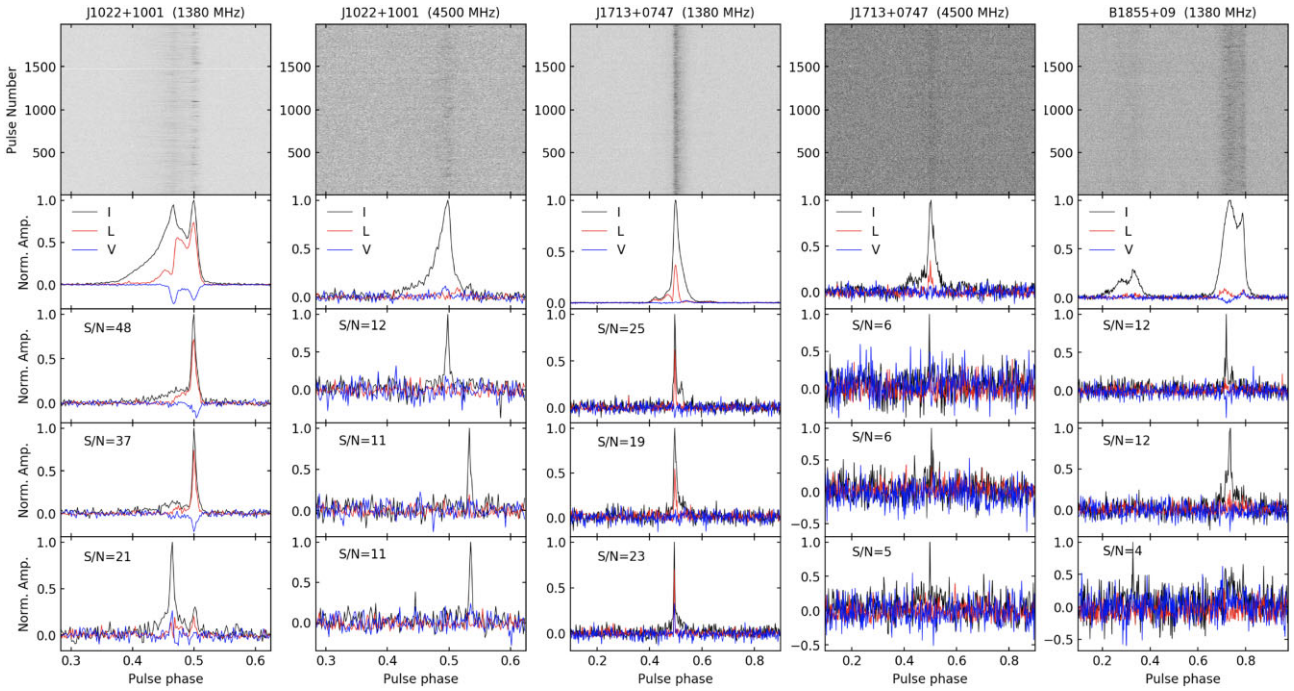

Figure 1. Multifrequency single pulse observations of PSRs J1022+1001, J1713+0747, and B1855 + 09 at observing frequency 1.38 and 4.5 GHz (see different columns). For each pulsar at each frequency, a sequence of 2000 single pulses in grey scale (*top panel*) and the averaged profiles of each pulse sequence, including total intensity (*black*), linear (*red*), and circular (*blue*) polarization (*second panel from top*) are shown. Three highest S/N single-pulse profiles are shown from each observation (*bottom three panels*). A single pulse associated with the leading component of PSR J1022+1001 at 1.38 GHz with a low fraction of linear polarization is also shown. Two single pulses of PSR J1022+1001 at 4.5 GHz which appear at the small trailing component at phase ≈0.53 (away from the main component) are also shown.

3.1 Single-pulse properties

We analyse single-pulse properties of the five data sets. Single-pulse amplitude and S/N distributions are used to identify phenomenon such as giant pulses, which have flux density >10 × the mean flux density (Karuppusamy, Stappers & Lee 2012; Knight 2007). The S/N for each single-pulse is calculated as

$$S/N = \frac{I_{\rm peak}}{\sigma_{\rm p}} \tag{4}$$

where $I_{\rm peak}$ is the peak amplitude, and $\sigma_{\rm p}$ is the off-pulse standard deviation of the pulse profile. The number and the fraction of detected single pulses (S/N > 5) is listed in Table 2.

3.2 Single-pulse polarimetry

Stokes parameters I, Q, U, V describe the polarization of electromagnetic waves, such that I is the total intensity, Q and U describe the intensity of linear polarization L as $L = \sqrt{Q^2 + U^2}$, and V is the intensity of circular polarization (see Lorimer & Kramer 2012). The polarization position angle is defined as PPA $= 0.5 \tan^{-1}$(U/Q).

3.3 Pulse phase jitter

As demonstrated by Shannon & Cordes (2012), timing residuals due to pulse-to-pulse jitter are expected to be correlated across radio frequency. For average profiles formed with N pulses, the root-mean-square (rms) residuals due to jitter noise, $\sigma_J(N)$, is quantified as the quadrature difference between the measured rms timing residuals, $\sigma_{\rm obs}(N)$, and the expected rms timing residuals from radiometer noise only, $\sigma_{\rm rad}(N)$, such that (Shannon & Cordes 2012)

$$\sigma_J(N)^2 = \sigma_{\rm obs}(N)^2 - \sigma_{\rm rad}(N)^2. \tag{5}$$

In order to determine the effect of jitter, composite profiles were formed with N = 50, 100, 200, 500, and 1000 pulses averaged together. For these various N values, $\sigma_{\rm obs}(N)$ was calculated from the timing residuals of the measured TOAs (obtained as described in Section 2) and $\sigma_{\rm rad}(N)$ was calculated from simulated profiles of similar S/N levels as the composite profiles (Downs & Reichley 1983). The simulated profiles were constructed by adding white noise to a noise-free template with signal-to-noise drawn from the signal-to-noise distribution of the observed composite profiles. We note that the simulated data set does not contain uncertainties due to profile shape variations or any other phenomena. The rms residuals due to jitter noise were determined from equation (5) for various N values.

Timing residuals due to jitter noise are correlated between sub-bands. The band may be split into several sub-bands and the correlation may be calculated between adjacent sub-bands (Parthasarathy et al. 2021). Following Shannon & Cordes (2012), we calculate the rms due to jitter by correlating timing residuals from the top and bottom halves of the band as $\sigma_j = \sqrt{\rm CCF(0)}$. Here, CCF(0) is the zero-lag value of the cross-correlation function. A different template profile was used for each sub-band.

4 RESULTS

In this section, we first present overall single-pulse total intensity, polarimetry, and jitter results and then present the results for individual pulsars in subsections.

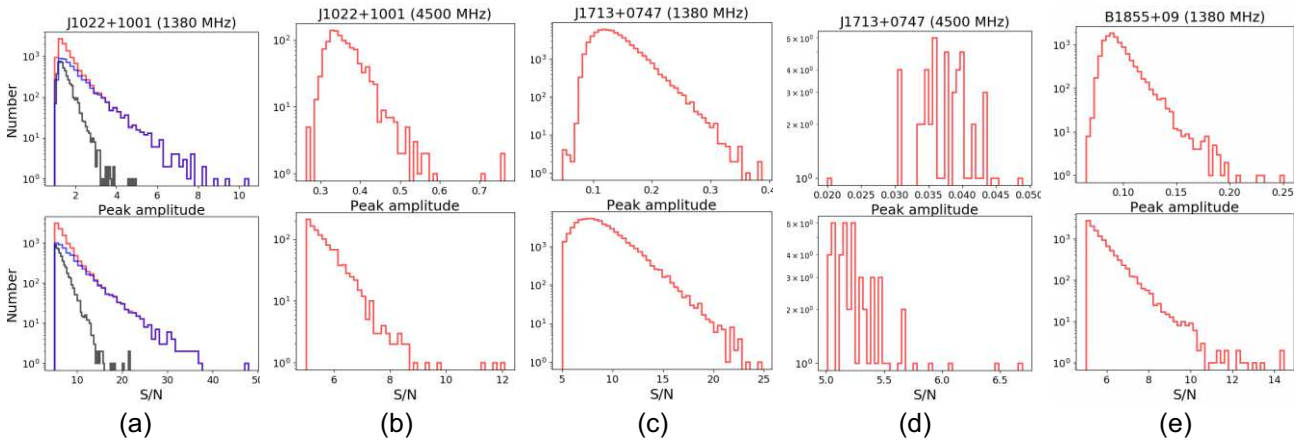

Figure 2. Histograms of peak amplitude (top) and S/N (bottom) of PSR J1022+1001 at 1.38 GHz (a) and 4.5 GHz (b), PSR J1713+0747 at 1.38 GHz (c), and 4.5 GHz (d), and PSR B1855+09 at 1.38 GHz (e). For PSR J1022+1001 at 1.38 GHz, the histograms of single-pulses associated with the leading (black) and trailing (blue) components are also shown separately in addition to the histograms of all single pulses (red). The brightest seem to correspond to the trailing component.

4.1 Single-pulse properties

Single pulses of S/N $>$ 5 are detected for PSRs J1022+1001 and J1713+0747 at 1.38 and 4.5 GHz, and for B1855+09 at 1.38 GHz. The 2.3 GHz data set of B1855+09 does not show detectable single pulses. To the best of our knowledge, this is the first report of the detection of single pulses at frequencies >2 GHz in MSPs.

Fig. 1 shows a single-pulse sequence (a stack of individual pulses in time versus pulse–phase), the total intensity and polarization profiles (see Section 3.2 for polarimetry) of averaged data and the three highest S/N individual single pulses from each data set. Fig. 2 shows the histograms of peak pulse amplitude distribution and the S/N distribution of single pulses of PSRs J1022+1001, J1713 + 0747, and B1855+09 at frequencies 1.38 and 4.5 GHz.

Fig. 3 shows the single-pulse equivalent width versus S/N. Overall, single pulses with higher S/N seem to be narrower than the ones with smaller S/N at 1.38 GHz, as shown in Fig. 3. In general, Gaussians or a series of Gaussians are fit to pulse profiles to estimate the width. The equivalent width method is better for automated calculation for many pulses, where goodness of fit is difficult to ascertain for each pulse, and to facilitate width measurements for weak pulses. At low S/N, the true width may be difficult to measure resulting in large width estimates. In Fig. 3, we plot width measurements determined with $>3\sigma$ significance.

4.2 Polarimetry

Fig. 4 shows the histograms of single-pulse linear and circular polarization fraction at the peak. The bias in L has been removed according to Everett & Weisberg (2001). Table 3 lists the linear and circular polarization fraction of the average profiles and the peak of the distributions of single-pulse polarization fractions shown in Fig. 4. The error on the polarization fraction of the average profile are obtained by using the standard deviation of I, L, and V across the profile and applying error propagation.

Phase resolved histograms of the PPA for single-pulse data were obtained using PSRSPA routine in PSRCHIVE. Fig. 5 shows the logarithm distribution of single-pulse PPA as a function of pulse phase along with the PPA of the average profile. The histogram is weighted by the total intensity.

4.3 Pulse phase jitter

Fig. 6 shows the correlation between the timing residuals from the top and bottom halves of the band, for 1000-pulse averages, along with the best-fitting line whose slope should be ideally be unity. The slopes of the best-fitting lines for the three pulsars are listed in Table 4. Table 4 also lists the zero lag value of the cross-correlation function CCF(0), rms timing residuals $\sigma_{\rm obs}$ for 1000-pulse averages, the reduced chi-square of the timing residuals (χ^2_r), the TOA error from radiometer noise $\sigma_{\rm rad}$, rms residuals due to jitter calculated from equation (5), the best-fitting parameters of the line $\sigma_J(N)$ versus N, and rms residuals due to jitter scaled to one hour. The rms residuals due to jitter for one hour averages were determined from the parameters of the best-fitting line to $\sigma_J(N)$ versus N such that $\sigma_J(N) = A\,N^{\beta}$, as shown in the bottom panel of Fig. 6. The error on the jitter level scaled to one hour is obtained by applying error propagation to $\sigma_J(N) = A\,N^{\beta}$. The quoted error bars correspond to 1σ level.

In the quadrature difference method, measuring the radiometer noise component accurately is important to get a reliable estimate for jitter noise since the data sets at higher frequencies are in general of low S/N. Higher S/N for these pulsars would not be achievable with any other existing telescope at 4.5 GHz. A comparison of the jitter level from the cross-correlation method and quadrature difference ($\sigma_{\rm j,\,CCF}$ and σ_j in Table 4) between the observed and simulated rms timing residuals shows that the values are comparable (within a factor of $\lesssim$1.1) in all data sets at 1.38 GHz. The inconsistencies at 4.5 GHz in both data sets of J1022+1001 and J1713+0747 could perhaps be because the radiometer noise component is underestimated or because jitter is decorrelated across the band (e.g. Parthasarathy et al. 2021).

4.4 PSR J1022+1001

As shown in Fig. 1, PSR J1022+1001 shows a double-peaked profile with a highly linearly polarized ($\approx$ 74 per cent) trailing component at 1.38 GHz, as also noted previously (Hotan, Bailes & Ord 2004; Liu et al. 2015). At 4.5 GHz, the leading component has reduced in amplitude with a more prominent trailing component which is only $\sim$3 per cent linearly polarized. While the percentage of circular polarization is 18 per cent at 1.38 GHz (under the leading

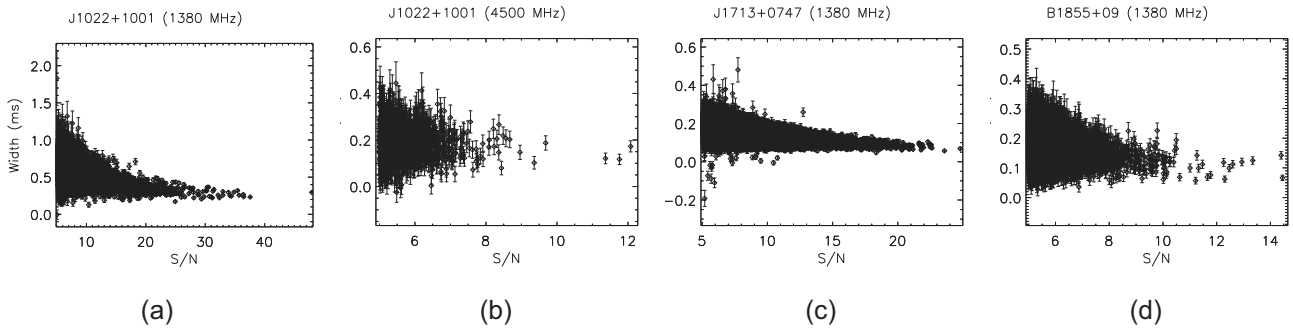

Figure 3. Measured single-pulse equivalent width and S/N values for PSR J1022+1001 at 1.38 GHz (a) and 4.5 GHz (b), PSR J1713+0747 at 1.38 GHz (c), and PSR B1855+09 at 1.38 GHz (d). The S/N cutoff is used to show only measurements $>3\sigma$. Widths of PSR J1713+0747 single pulses at 4.5 GHz are not shown due to the small fraction of detected pulses with S/N > 5.

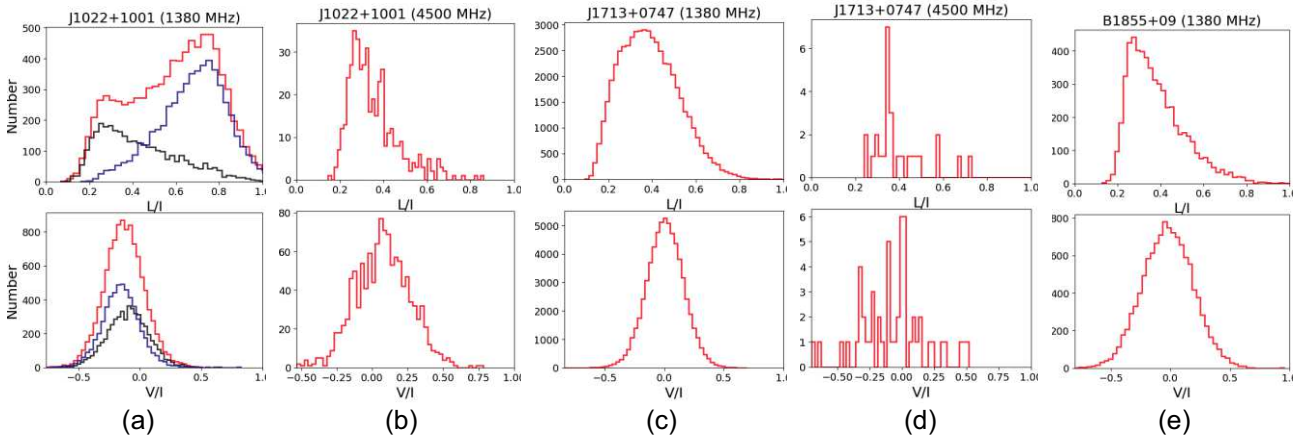

Figure 4. Histograms of linear polarization (top) and circular polarization (bottom) for PSR J1022+1001 at 1.38 GHz (a) and 4.5 GHz (b), PSR J1713+0747 at 1.38 GHz (c), and 4.5 GHz (d), and PSR B1855+09 at 1.38 GHz (e). For PSR J1022+1001 at 1.38 GHz, the histograms of single-pulses associated with the leading (black) and trailing (blue) components are also shown separately. Single pulses associated with the trailing component show a higher fractional linear polarization than those associated with the leading component.

Table 3. Polarization parameters: percentage fractional linear and circular polarization of the average profile and the peak of the histograms of linear and circular polarizations shown in Fig. 4.

Pulsar	Frequency (MHz)	L_{av}/I_{av}	V_{av}/I_{av}	L/I	V/I
J1022+1001	1380	73.9 ± 0.2	−18.0 ± 0.2	25.9 ± 1.5, 73.8 ± 1.5	−14.6 ± 1.6
J1022+1001	4500	3.2 ± 0.3	6.9 ± 0.4	26.5 ± 0.7	6.0 ± 1.3
J1713+0747	1380	36.6 ± 0.5	0.9 ± 0.5	36.3 ± 0.9	− 0.5 ± 1.5
J1713+0747	4500	30.1 ± 0.6	− 1.4 ± 0.8	34.5 ± 0.8	− 0.6 ± 1.2
B1855+09	1380	6.6 ± 0.1	− 3.5 ± 0.2	27.3 ± 0.9	− 4.6 ± 1.7

Note. For PSR J1022+1001 at 1.38 GHz the peak fractional linear polarization for leading and trailing components are listed separately.

component), it is almost negligible at 4.5 GHz. The PPA of the average profile follows an S-shaped swing with a 'notch' at the first peak (Fig. 4a) as also reported by Kramer et al. (1999). This pulsar shows long-term profile variations (Kramer et al. 1999), which have been attributed to improper polarization calibration in the past (van Straten 2013), even though more recent studies suggest that intrinsic effects may likely be at play (Liu et al. 2015; Padmanabh et al. 2021). By using the measured flux densities given in Table 2, we measure a spectral index of −1.43 ± 0.24, consistent (within errors) with the published value of −1.7 ± 0.1 (Kramer et al. 1998). Since the observed flux density of this pulsar is known to vary significantly due to diffractive scintillation (Liu et al. 2015; Shannon et al. 2014), flux density measurements over multiple epochs are needed for accurate spectral index measurements.

We do not see evidence for giant pulses. However, the data set consists of very bright pulses of (S/N ≈ 30), which are ≈×5 the mean S/N. At 4.5 GHz, some bright single pulses appear at phase ≈0.53 (phase ≈0.03 away from the main component) as shown in Fig. 1.

The brightest single pulses of PSR J1022+1001 at 1.38 GHz are highly linearly polarized, as also noted in other studies (Liu et al. 2015). We find that the single-pulse linear polarization distribution

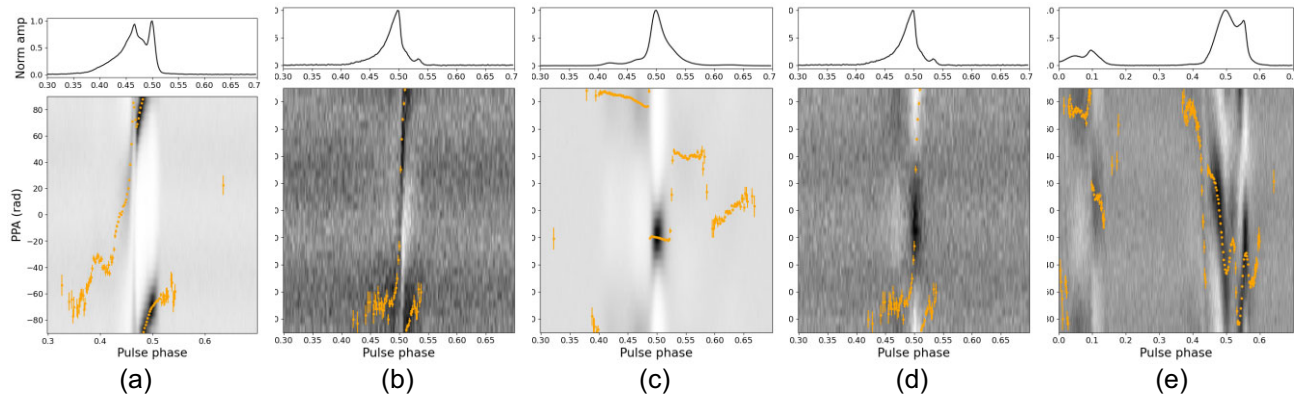

Figure 5. The total intensity average profile of the full data set (top) and the single-pulse PPA distribution (bottom grey scale) of for PSR J1022+1001 at 1.38 GHz (a) and 4.5 GHz (b), PSR J1713+0747 at 1.38 GHz (c), and 4.5 GHz (d), and PSR B1855+09 at 1.38 GHz (e). The PPA of the average profile (orange) is also marked.

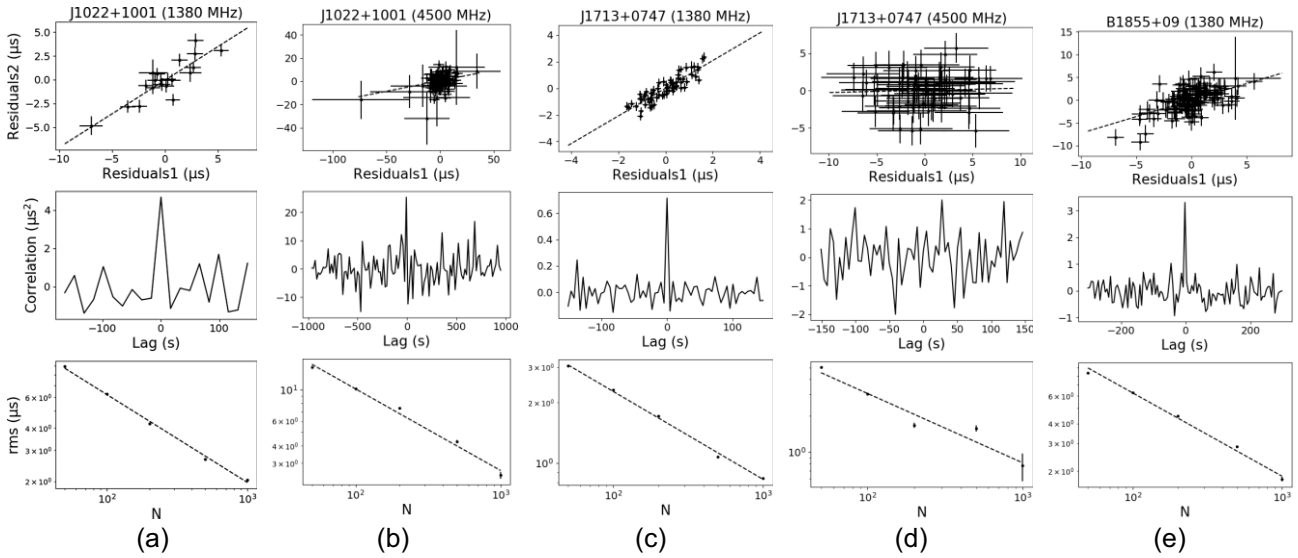

Figure 6. Correlation between TOAs of top and bottom halves of the band for 1000-pulse averages along with the best-fitting line (top), the cross correlation function (middle), and the rms timing residuals from jitter versus the number of pulses averaged (bottom) for PSR J1022+1001 at 1.38 GHz (a) and 4.5 GHz (b), PSR J1713+0747 at 1.38 GHz (c), and 4.5 GHz (d), and PSR B1855+09 at 1.38 GHz (e). In the bottom plots the best-fitting line to jitter noise is shown by the dashed line. The correlation is negligible for both PSRs J1022+1001 and J1713+0747 at 4.5 GHz for 1000-pulse averages likely due to radiometer noise in profiles.

Table 4. Phase jitter analysis: Pulsar name, frequency, the slope of the best fit to the timing residual correlation for 1000-pulse averages (m -see the top panel of Fig. 6), the corresponding zero-lag value of the CCF (CCF(0)), rms residuals due to jitter from the CCF ($\sigma_{\rm j,\,CCF}$), measured rms timing residuals ($\sigma_{\rm obs}$), the reduced chi-square of the timing residuals (χ^2_r), rms residuals due to radiometer noise ($\sigma_{\rm rad}$), rms residuals due to jitter ($\sigma_{\rm j}$) from the quadrature difference between $\sigma_{\rm obs}$ and $\sigma_{\rm rad}$, jitter scaling parameters (A, β – see the text), and $\sigma_{\rm j}$ scaled to one hour ($\sigma_{\rm j,\,1\,hr}$).

Pulsar	Frequency (MHz)	m	CCF(0) (μs^2)	$\sigma_{\rm j,\,CCF}$ (ns)	$\sigma_{\rm obs}$ (ns)	χ^2_r	$\sigma_{\rm rad}$ (ns)	$\sigma_{\rm j}$ (ns)	(A, β)	$\sigma_{\rm j,\,1\,hr}$ (ns)
J1022+1001	1380	0.71	4.7	2164	2086	16.1	467	2033	(61.10,−0.50)	135 ± 29
J1022+1001	4500	0.18	25.3	5033	4502	1.69	3764	2469	(146.4,−0.58)	117 ± 52
J1713+0747	1380	1.04	0.72	846	851	49.9	121	842	(17.03,−0.44)	45 ± 7
J1713+0747	4500	0.03	0.22	473	1939	1.30	1779	772	(43.15,−0.57)	17 ± 22
B1855+09	1380	0.80	3.31	1819	2003	7.87	914	1782	(70.39,−0.53)	60 ± 25

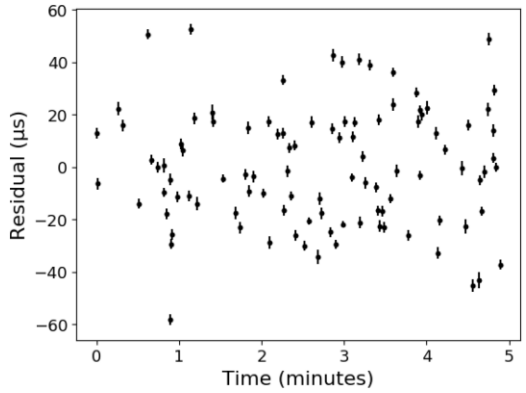

Figure 7. The rms timing residuals of PSR J1022+1001 single-pulses of S/N > 25 at 1.38 GHz.

of PSR J1022+1001 at 1.38 GHz shows two peaks (see Fig. 4). Single pulses associated with the leading component of the average profile tend to have a low-linear polarization fraction (average $L/I \approx 0.3$) compared to the single pulses associated with the second peak (average $L/I \approx 0.7$). As evident from Table 3 and Fig. 4, in general, the fraction of linear polarization is reduced at higher frequencies. The brightest single pulses at 4.5 GHz (of S/N > 5 which we consider in our analysis) show higher fractional L/I compared to the average profile.

The rms timing residual due to pulse-to-pulse jitter at 1.38 GHz, scaled to one hour, is 135 ± 29 ns. This is consistent (within the 2σ error) with the 67 ± 9 reported by Feng et al. (2020) or ≈700 ns for 1-min integration (≈90 ns for one hour) reported by Liu et al. (2015) at 1.38 GHz, but lower than the Shannon et al. (2014) value of 290 ± 15 and 269 ± 4 ns of Lam et al. (2019). The level of jitter at 4.5 GHz, scaled to one hour, is 117 ± 52 ns, which is consistent with that at 1.38 GHz within errors.

Following Liu et al. (2015) and Feng et al. (2020), we measured the rms timing residuals of single pulses from the leading and trailing component separately. Considering all single pulses with S/N > 5 results in rms timing residuals of ≈ 70 and ≈ 43 μs for leading and trailing components, respectively. For TOA calculation, the template profile was created by averaging over all pulses of S/N > 5 within each component. Liu et al. (2015) find rms timing residuals of 4.3 μs for averages of 30 trailing component sub-pulses of S/N > 5, which converts to $4.3 \times \sqrt{30} \approx 23$ μs at the single–pulse level. The reason for higher rms timing residuals in our data set could be the higher levels of jitter compared to Liu et al. (2015) possibly due to the pulsar showing variable jitter noise or the difference in radiometer noise.

We also measured the rms timing residuals of single pulses within S/N ranges of 5 < S/N < 15, 15 < S/N < 25, and S/N > 25. As shown in Fig. 7, the rms timing residual using the brightest pulses (S/N > 25) is ≈ 22 μs. For TOA calculation, the template profile was created by averaging over all pulses within each S/N range. Scaling the rms of ≈ 2.09 μs from 1000-pulse averages (Table 4) simply as $\sigma_{\rm obs} \propto 1/\sqrt{N_{\rm p}}$ (e.g. Shannon & Cordes 2012), where $N_{\rm p}$ is the number of pulses in the average profile, the expected single-pulse RMS is ≈ 66 μs. So timing just the brightest pulses gives a factor of ≈3 improvement. The vast majority of pulses (99 per cent) within S/N > 25 range appear at the trailing component. Using single pulses within the S/N ranges of 5 < S/N < 15 and 15 < S/N < 25 yields rms timing residuals of 69 and 74 μs, respectively. The higher rms residuals in pulses within the 15 < S/N < 25 range could be due to a small percentage (3.7 per cent) of pulses occurring at the leading component while the rest occur at the trailing component. When these trailing edge pulses are removed, the rms timing residuals within 15 < S/N < 25 reduce to 28 μs.

4.5 PSR J1713+0747

PSR J1713+0747 is a binary pulsar which shows relativistic effects (Camilo, Foster & Wolszczan 1994; Splaver et al. 2005). PSR J1713+0747 shows a multicomponent average profile with a significant linear polarization (≈ 37 per cent) at the peak at 1.38 GHz, consistent with previous studies (e.g. Yan et al. 2011). This is reduced but still significant (≈ 30 per cent) at 4.5 GHz. We measure a spectral index of −1.69 ± 0.38 using the flux densities obtained at 1.38 and 4.5 GHz (see Table 2), which is consistent (within errors) with the published value of −1.5 ± 0.1 (Kramer et al. 1998). The more prominent outer components at 4.5 GHz compared to at 1.38 GHz (at phases ≈0.42 and 0.47), also reported in Kijak et al. (1997), are evident in our data (see Fig. 1). The faint emission component at phase ≈0.63 at 1.38 GHz is also more prominent at 4.5 GHz. Previous studies have reported a jitter contribution of ≈35 ± 0.8 ns to rms timing residuals residuals in one hour of integration of this pulsar (Shannon et al. 2014; Liu et al. 2016), consistent (within the 2σ error) with the 45 ± 7 ns that we find at 1.38 GHz. At 4.5 GHz, the lack of correlation (see the top two panels of Fig. 6d) and the large error in the quadrature difference method point to jitter being not constrained.

Although, the data set consists of very bright pulses of S/N ≈ 20, we do not see evidence for giant pulses. The fraction of single pulses detected at 4.5 GHz is very small, which stops us from performing detailed analysis.

The PPA of the average profile shows 90° jumps (see Fig. 5) that indicate the presence of OPMs (Xilouris et al. 1998). Indeed OPMs have been detected in this pulsar at 1.38 GHz in Large European Array for Pulsars (LEAP) data (Liu et al. 2016). A faint offset in the PPA distribution of single pulses at phase ≈0.5 is noted in Fig. 5, hinting at an OPM for this pulsar.

4.6 PSR B1855+09

PSR B1855+09 is a relativistic binary which has both main pulse (MP) and an interpulse (IP), with both showing a double-peaked structure and weak (≈ 7 and ≈ 2 per cent in the MP and IP, respectively) linear polarization consistent with previous studies (Kramer et al. 1998). The PPA of the average profile in the MP does not follow an S-shaped swing. The discontinuities in the PPA curve of the IP is non-orthogonal and consistent with Xilouris et al. 1998 even though some studies have noted orthogonal transitions (Yan et al. 2011). Based on the measured flux densities at 430 MHz and 1.38 GHz, we measure a spectral index of −0.6 ± 0.1, slightly flatter than the published value of −1.3 ± 0.2 (Kramer et al. 1998). The flux density measurement at 2 GHz is unusually low, likely due to the very low S/N of the data set or scintillation, and therefore has not been included in the spectral index measurement. We also note that our data are only polarization calibrated, and therefore these flux density measurements may not be precise. Therefore, we again emphasise that multiepoch flux density measurements may give a better estimate of the the spectral index. Also, note that the MSP spectral index is not well constrained (Bates, Lorimer & Verbiest 2013; Kuniyoshi et al. 2015). We find that the rms timing residual due to jitter, scaled to one hour, is 60 ± 25 ns (70 ± 11 μs at the single-pulse level). This is roughly consistent within the 3σ confidence interval of 90–115 μs published in Lam et al. (2019).

Single pulses of PSR B1855+09 at 1.38 GHz also show higher fractional *L*/*I* compared to the average profile. We also note that even though the flux density at 430 MHz is high, the expected S/N of a single pulse is low and therefore single pulses are not detected at these low frequencies possibly due to the high sky temperature. For Arecibo observations (parameters listed in Table 2), the expected S/N, for B1855+09 at 430 MHz, calculated from the radiometer equation,

$$S/N = \frac{G\sqrt{N_{\rm p} W\, \Delta\nu}\, S_{\rm peak}}{T_{\rm sys}} \quad (6)$$

is <5. Here $S_{\rm peak}$ is the peak flux density (estimated using the mean flux density and duty cycle) and we assume that the single-pulse width is $W \approx 0.17$ ms, which is the mean single–pulse equivalent width of B1855+09 at 1.38 GHz.

A few single pulses associated with the IP are detected with low S/N (example shown in the bottom panel of Fig. 1). However, due to their low S/N, only single-pulses associated with the MP are used for detailed analysis.

5 CONCLUSION AND DISCUSSION

We have studied the total intensity properties, single-pulse polarimetry and pulse phase jitter of MSPs J1022+1001, J1713+0747, B1855+09 at multiple frequencies. On the single-pulse front, we do not detect giant pulses, but we still find bright single pulses at 1.38 GHz for all three MSPs. Overall, single pulses with higher S/N seems to be narrower than the ones with smaller S/N at 1.38 GHz, as shown in Fig. 3.

As evident from Table 3, in general, the fraction of linear polarization in the average profile is reduced at higher frequencies. This may be consistent with similar findings of normal pulsars that show that average profiles are depolarized at higher frequencies (e.g. Xilouris et al. 1996; Johnston, Karastergiou & Willett 2006). This is because high frequency emission arises closer to the pulsar surface where the magnetic field deviates from a dipole field resulting in superposition of modes and hence significant depolarization (e.g. McKinnon 1997; Wang, Wang & Han 2015; van Straten & Tiburzi 2017). Dai et al. (2015) reported this trend for PSRs J1022+1001, J1713+0747, and B1855+09 using 1.38 and 3 GHz observations. Our results confirm that this trend continues at 4.5 GHz for PSRs J1022+1001 and J1713+0747. Single pulses from PSR J1022+1001 at 4.5 GHz and PSR B1855+09 at 1.38 GHz show high fractional linear polarization than the average profile. This could be because bright pulses show more fractional polarization or due to depolarization from averaging.

In our data set, the fraction of single pulses detected at 4.5 GHz is very small, which prevents us from performing detailed analysis. Sensitive observations are needed to better understand single-pulse phenomena at higher frequencies. For example, the expected S/N at 4.5 GHz for a FAST-like telescope (even though cannot observe at frequencies >2 GHz with current system), with a gain of G = 18 K Jy^{-1}, $T_{\rm sys}$ = 20 K, BW = 800 MHz (Li & Pan 2016), would be a factor of ≈6 better than our data. Upcoming facilities with high sensitivity and frequency coverage should facilitate multifrequency single-pulse studies of pulsars.

The jitter levels ($\sigma_{\rm j}$) we find are consistent for PSRs J1022+1002 (Liu et al. 2015; Feng et al. 2020; Parthasarathy et al. 2021), PSR J1713+0747 (Shannon et al. 2014; Liu et al. 2016), and PSR B1855+09 (Lam et al. 2019) at 1.38 GHz. But the fact that PSR J1022+1001 has lower values of jitter recorded in other studies (Shannon et al. 2014; Lam et al. 2019) could indicate variable jitter noise. The contribution to the pulsar noise budget from jitter at 4.5 and 1.38 GHz are consistent (within the 2σ error) for PSR J1022+1001. The level of jitter from the cross-correlation method ($\sigma_{\rm j,\,CCF}$) and the quadrature difference method ($\sigma_{\rm j}$ in Table 4) are comparable at 1.38 GHz. At 4.5 GHz, either the radiometer noise component is underestimated or jitter is decorrelated across the band (e.g. Parthasarathy et al. 2021). Jitter noise is expected to be lower at higher frequencies due to narrower profiles and lower flux densities, though previous studies have shown that not all pulsars follow this trend (Shannon et al. 2014; Lam et al. 2019). While some MSPs used in PTAs show levels of jitter as low as tens of ns per hour, others (which have large pulse widths and small periods) show levels of jitter amounting to hundreds of ns per hour (Shannon et al. 2014; Parthasarathy et al. 2021). Lam et al. (2019) has found that 43 pulsars out of a sample of 48 shows significant jitter and that 30 of those show significant frequency dependence. The general notion is that jitter noise should be detectable in all MSPs if observed with adequate sensitivity (Shannon et al. 2014), and therefore accurately including jitter in noise modelling is important in high-precision pulsar timing. It also represents a fundamental lower limit on the timing precision achievable for individual MSPs.

We also find that timing only the brightest pulses of PSR J1022+1001 results in an improvement in rms timing residuals by a factor of ≈3 than what is expected by scaling timing properties derived from all single pulses. However, given relative paucity of such bright pulses, the timing may not be improved when compared to fully integrating all available data in a fixed observation time. We note that previous studies have found that selective timing does not yield a significant improvement in timing (Osłowski et al. 2014; Feng et al. 2020). The first of these studies reported reduced χ^2 of the timing residuals when selectively integrating only weaker pulses, as well as a minor improvement to timing when using brighter pulses. The reason for our improvement in timing could be because we only include the brightest pulses with a large trailing component and remove the pulses that have a large leading component and thereby selecting only the brightest pulses which appear within the narrow phase range of the trailing component. Our very short data set prevents us from timing using integrated profiles of selected bright pulses, but this is an important avenue for further exploration. Therefore, further investigation is needed to see if selective timing yields an improvement for integrated profiles formed with bright pulses within a given component of the profile.

ACKNOWLEDGEMENTS

The authors thank Hector Hernandez, Phil Perrillat, and other Arecibo Observatory staff for help with scheduling, observation support, and data quality checks. The Arecibo Observatory is a facility of the National Science Foundation operated under cooperative agreement by the University of Central Florida in alliance with Yang Enterprises, Inc. and Universidad Metropolitana. The authors also thank the anonymous referee for the constructive remarks on this manuscrpt. NP, BPP, and MAM are members of the NANOGrav Physics Frontiers Center, supported by NSF awards PHY-1430284 and PHY-2020265.

DATA AVAILABILITY

The data underlying this article will be shared on reasonable request to the corresponding author.

REFERENCES

Alam M. D. F. et al., 2021, ApJS, 252, 48
Arzoumanian Z. et al., 2018, ApJS, 235, 41
Backer D. C., 1970, Nature, 228, 1297
Backer D. C., 1973, ApJ, 182, 245
Backer D. C., Rankin J. M., 1980, ApJS, 42, 143
Backer D. C., Rankin J. M., Campbell D. B., 1976, Nat, 263, 202
Bates S. D., Lorimer D. R., Verbiest J. P. W., 2013, MNRAS, 431, 1352
Britton M. C., 2000, ApJ, 532, 1240
Brook P. R. et al., 2018, ApJ, 868, 28
Camilo F., Foster R. S., Wolszczan A., 1994, ApJ, 437, L39
Cocke W. J., 1973, ApJ, 184, 291
Cordes J. M., Shannon R. M., 2010, preprint (arXiv:1010.3785)
Cordes J. M., Rankin J., Backer D. C., 1978, ApJ, 223, 961
Cordes J. M., Weisberg J. M., Hankins T. H., 1990, AJ, 100, 1882
Dai S. et al., 2015, MNRAS, 449, 3223
De K., Gupta Y., Sharma P., 2016, ApJ, 833, L10
Desvignes G. et al., 2016, MNRAS, 458, 3341
Downs G. S., Reichley P. E., 1983, ApJS, 53, 169
Edwards R. T., Hobbs G. B., Manchester R. N., 2006, MNRAS, 372, 1549
Enoto T. et al., 2021, Sci., 372, 187
Everett J. E., Weisberg J. M., 2001, ApJ, 553, 341
Feng Y. et al., 2020, ApJ, 908, 7
Frake F. D., Craft H. D., 1968, Nature, 220, 231
Gentile P. A. et al., 2018, ApJ, 862, 20
Gil J. A., Snakowski J. K., 1990, AAP, 234, 269
Gil J. A., Melikidze G. I., Mitra D., 2002, A&A, 388, 235
Goldreich P., Julian W. H., 1969, ApJ, 157, 869
Hankins T. H., Eilek J. A., 2007, ApJ, 670, 693
Haslam C. G. T., Salter C. J., Stoffel H., Wilson W. E., 1982, A&AS, 47, 1
Heiles C., Campbell D. B., 1970, Nature, 226, 529
Hobbs G. B., Edwards R. T., Manchester R. N., 2006, MNRAS, 369, 655
Hotan A. W., Bailes M., Ord S. M., 2004, MNRAS, 355, 941
Hotan A. W., van Straten W., Manchester R. N., 2004, PASA, 21, 302
Hotan A. W., Bailes M., Ord S. M., 2006, MNRAS, 369, 1502
Jenet F. A., Anderson S. B., Kaspi V. M., Prince T. A., Unwin S. C., 1998, ApJ, 498, 365
Johnston S., Karastergiou A., Willett K., 2006, MNRAS, 369, 1916
Kalapotharakos C., Wadiasingh Z., Harding A. K., Kazanas D., 2021, ApJ, 907, 63
Karuppusamy R., Stappers B. W., Lee K. J., 2012, A&A, 538, A7
Kerr M. et al., 2020, PASA, 37, e020
Kijak J., Kramer M., Wielebinski R., Jessner A., 1997, A&A, 318, L63
Knight H. S., 2007, MNRAS, 378, 723
Kramer M., Xilouris K. M., Lorimer D. R., Doroshenko O., Jessner A., Wielebinski R., Wolszczan A., Camilo F., 1998, ApJ, 501, 270
Kramer M. et al., 1999, ApJ, 520, 324
Kuniyoshi M., Verbiest J. P. W., Lee K. J., Kramer M., Noutsos A., 2015, MNRAS, 453, 828
Lam M. T. et al., 2019, ApJ, 872, 17
Li D., Pan Z., 2016, Radio Sci., 51, 1060
Liu K., Verbiest J. P. W., Kramer M., Stappers B. W., van Straten W., Cordes J. M., 2011, MNRAS, 417, 2916
Liu K. et al., 2015, MNRAS, 449, 1158
Liu K. et al., 2016, MNRAS, 463, 3239
Lorimer D. R., Kramer M., 2012, in Lorimer D. R., Kramer M., eds, Handbook of Pulsar Astronomy. Cambridge Univ. Press, Cambridge
Lyne A. G., Smith F. G., 1989, MNRAS, 237, 533
Lyne A., Hobbs G., Kramer M. et al., 2010, Sci., 329, 408
Machabeli G. Z., Usov V. V., 1979, Sov. Astron. Lett., 5, 238
McKee J. W. et al., 2019, MNRAS, 483, 4784
McKinnon M. M., 1997, ApJ, 475, 763
McKinnon M. M., Stinebring D. R., 2000, ApJ, 529, 435
Melrose D. B., 1992, in Hankins T. H., Rankin J. M., Gil J. A., eds, IAUColloq. 128, The Magnetospheric Structure and Emission Mechanismsof Radio Pulsars. Pedagogical Univ. Press, Zielona, Gora, p. 306
Melrose D. B., 1995, JA&A, 16, 137
Melrose D. B., Gedalin M. E., 1999, ApJ, 521, 351
Melrose D. B., Rafat M. Z., Mastrano A., 2021, MNRAS, 500, 4530
Mitra D., Rankin J. M., 2011, ApJ, 727, 92
Mitra D., Gil J., Melikidze G. I., 2009, ApJ, 696, L141
Noutsos A. et al., 2015, A&A, 576, 26
Osłowski S., van Straten W., Demorest P., Bailes M., 2013, MNRAS, 430, 416
Osłowski S., van Straten W., Bailes M., Jameson A., Hobbs G., 2014, MNRAS, 441, 3148
Padmanabh P. V., Barr E. D., Champion D. J., Karuppusamy R., Kramer M., Jessner A., Lazarus P., 2021, MNRAS, 500, 1178
Parthasarathy A. et al., 2021, MNRAS, 502, 407
Perera B. B. P. et al., 2018, MNRAS, 478, 218
Perera B. B. P. et al., 2019, MNRAS, 490, 4666
Radhakrishnan V., Cooke D. J., 1969, Astrophys. Lett., 3, 225
Rankin J. M., 1983a, ApJ, 274, 333
Rankin J. M., 1983b, ApJ, 274, 359
Rankin J. M., 1986, ApJ, 301, 901
Reardon D. J. et al., 2016, MNRAS, 455, 1751
Romani R. W., Johnston S., 2001, ApJ, 557, L93
Ruderman M. A., Sutherland P. G., 1975, ApJ, 196, 51
Shannon R. M., Cordes J. M., 2012, ApJ, 761, 8
Shannon R. M. et al., 2014, MNRAS, 443, 1463
Simard-Normandin M., Kronberg P. P., 1980, ApJ, 242, 74
Splaver E. M., Nice D. J., Stairs I. H., Lommen A. N., Backer D. C., 2005, ApJ, 620, 405
van Straten W., 2006, ApJ, 642, 1004
van Straten W., 2013, ApJS, 204, 13
van Straten W., Bailes M., 2011, PASA, 28, 1
van Straten W., Tiburzi C., 2017, ApJ, 835, 293
Wahl H. M. et al., 2021, ApJ, 926, 24
Wang P. F., Wang C., Han J. L., 2015, MNRAS, 448, 771
Xilouris K. M., Kramer M., Jessner A., Wielebinski R., Timofeev M., 1996, A&A, 309, 481
Xilouris K. M., Kramer M., Jessner A., von Hoensbroech A., Lorimer D. R., Wielebinski R., Wolszczan A., Camilo F., 1998, ApJ, 501, 286
Xu H. et al., 2021, Astron. Telegram, 14642, 1
Yan W. M. et al., 2011, MNRAS, 414, 2087
You X. P., Coles W. A., Hobbs G. B., Manchester R. N., 2012, MNRAS, 422, 1160
Zhelezniakov V. V., Shaposhnikov V. E., 1979, Aust. J. Phys., 32, 49
Zhu W. W. et al., 2015, ApJ, 809, 41

This paper has been typeset from a TEX/LATEX file prepared by the author.